Available online at www.sciencedirect.com
SCIENCE DIRECT®

Journal of the European Ceramic Society 24 (2004) 3317–3326
www.elsevier.com/locate/jeurceramsoc

Effect of oxide dopants on densification, microstructure and mechanical properties of alumina-silicon carbide nanocomposite ceramics prepared by pressureless sintering

Sunil Kumar C. Pillai[1], Benoit Baron[2], Michael J. Pomeroy, Stuart Hampshire*

Materials and Surface Science Institute, University of Limerick, Limerick, Ireland

Abstract

The densification behaviour, microstructural development and mechanical properties of a 5 vol.% silicon carbide dispersed alumina nanocomposite were studied by incorporating six different oxide dopants (1 wt.%). It was found that MgO, Y_2O_3 and CeO_2 enhanced the densification of the nanocomposite, which can be explained by a liquid phase assisted sintering process. The yttria-doped nanocomposite could be pressureless sintered at 1550 °C. Doping with MgO or CeO_2 refines the grain size of the matrix alumina whereas yttria addition induces exaggerated grain growth. The Young's modulus, hardness, fracture toughness and erosive wear resistance were evaluated. Doped nanocomposites exhibit slightly lower Young's modulus and higher hardness values than that of the undoped nanocomposite. CeO_2 doping improves hardness and fracture toughness slightly whereas the improvement in erosive wear resistance was 2.5 times higher than the other nanocomposites. Improvements in properties are explained in terms of residual compressive stresses, grain refinement and grain boundary strengthening.

Keywords: Al_2O_3; Electron microscopy; Grain boundaries; Mechanical properties; Sintering; Wear resistance

1. Introduction

The first alumina–silicon carbide nanocomposites, produced mainly by hot-pressing, were reported to have improved microstructures and mechanical properties.[1–6] However, the improvements in mechanical properties (such as strength and fracture toughness) varied between the various researchers due to the differences in processing and testing conditions. In alumina–silicon carbide nanocomposites, most of the researchers observed a so-called intra/inter type of microstructure, that is, most of the SiC particles, typically less than 0.2 μm, were predominantly dispersed within the matrix grains but with some larger SiC particles at the grain boundaries and triple point junctions.[1,2,7–9] The most advantageous effect of SiC nanoparticles in an alumina matrix was proposed to be their ability to refine the microstructure of the nanocomposite by restricting grain growth of the matrix alumina, which was reflected in their improved mechanical properties.

It is, however, important to note that significant improvements in mechanical properties were generally observed only in nanocomposites prepared by hot pressing. In the case of pressureless sintering of the nanocomposites,[5,6,10–12] high temperatures (>1750 °C) were necessary in order to achieve near fully dense materials.

The ultimate properties of a material depend on the microstructures developed during sintering. Usually, undoped alumina is very difficult to sinter to theoretical density. The major factors which hinder the densification are abnormal grain growth and pore detachment from the grain boundaries during boundary migration, which effectively leaves the pores permanently trapped inside the grains.[13] Small amounts of dopants, such as MgO, can improve the densification and microstructural development of alumina.[14] Dopants can alter the boundary, lattice and surface diffusivities, leading to a change in boundary and pore mobilities. They can create drag forces on boundary motion by segregating to grain boundaries and, when segregation increases, they can pin the grain boundaries, thus inhibiting

* Corresponding author.
E-mail address: stuart.hampshire@ul.ie (S. Hampshire).
[1] Present address: Department of Materials Science and Engineering, University of Michigan, Ann Arbor, MI 48109, USA.
[2] Present address: 3M France, 59400 Tilloy-lez-Cambrai, France.

0955-2219/$ - see front matter © 2003 Elsevier Ltd. All rights reserved.
doi:10.1016/j.jeurceramsoc.2003.10.024

growth. If the solute concentration at the grain boundary is too great, it becomes oversaturated and a new phase is formed.[15] Bae and Baik[16] have shown that impurities, even at levels of <30 ppm, can have significant effects in ceramic systems.

The use of dopants has been carried out in nanocomposite systems by some researchers.[17–20] Wang et al.[17] observed that addition of 0–300 ppm MgO could significantly increase the sintered density of a pressureless sintered alumina–5 vol.% silicon carbide nanocomposite. Further addition of MgO up to 1000 ppm did not improve the density. This finding was supported by Jeong et al.[18] They proposed that MgO was likely to modify the grain boundary structure or the grain boundary phase in the nanocomposite. It was also observed that a small amount of Y_2O_3 could introduce exaggerated grain growth in the nanocomposite which can be controlled.[19] Borsa et al.[20] using dopants to provide conditions for liquid phase sintering, found that an alumina/silicon carbide nanocomposite could be hot-pressed to high densities at temperatures as low as 1300 °C. Hence, it is evident from these observations that doping can be a useful method to enhance the sinterability of alumina/silicon carbide nanocomposites.

Erosive wear rates for alumina–SiC nanocomposites (hot-pressed) have been measured by Davidge et al.[21] and compared with those for pure polycrystalline alumina (hot-pressed) of similar grain size. They observed significant increase in the wear resistance of the nanocomposite. It was suggested that the improvement in wear resistance could be attributed to the dislocation substructure formed in the nanocomposite and the inhibition of grain growth caused by the SiC nanophase. In another investigation using the same test method, Twigg et al.[22] found a lower wear rate for a series of alumina nanocomposites with 0.01 and 0.11 μm SiC dispersoids than with composites containing SiC particles larger than the matrix alumina grain size. In the nanocomposites, the predominant wear mechanisms were plastic dominated processes, while the conventional composites wore by micro-fracture, with the degree of fracture increasing with SiC particulate size.

Franco and Roberts[23] used a rotary jet slurry wear tester to evaluate the erosive wear of polycrystalline alumina. They observed that the weight loss of polycrystalline alumina and sapphire specimens due to normal particle impacts by SiC grits in water increased linearly with impacting time. The measured wear rate of polycrystalline alumina was grain-size-dependent, being about one order of magnitude greater for alumina of 14.1 μm grain size than for alumina of 1.2 μm grain size.

In the present study, detailed analyses were carried out on the effect of MgO, Y_2O_3 and CeO_2 on the densification, microstructural development and properties, particularly erosive wear resistance of pressureless sintered alumina–5 vol.% silicon carbide nanocomposites.

2. Experimental

Raw materials used for the preparation of undoped alumina–5 vol.% SiC nanocomposites (referred to hereafter as 'NC') were P172SB alumina (99.77%, Pechiney, France) and UF45 silicon carbide (Starck, Germany) powders. Impurities and characteristics of the raw materials as given by the manufacturers are shown in Table 1. Doped nanocomposites were prepared by adding 1 wt.% of the corresponding dopant, MgO, Y_2O_3 and CeO_2, added as nitrates, to the alumina–5 vol.% SiC nanocomposite (referred to as 1Mg–NC, 1Y–NC and 1Ce–NC). Fig. 1 shows the flow diagram for processing of the nanocomposites. Respective amounts of alumina and silicon carbide powders were attrition milled using silicon nitride balls (~1 mm diameter) and grinding chamber and using distilled water as the medium. For preparing doped nanocomposites, the nitrate of the corresponding dopant was first dissolved in distilled water and then added to the alumina–silicon carbide slurry in the attrition chamber. Attrition milling was carried out at 1000 rpm rotation speed for 2 h. The slurry was then dried using a freeze-drying

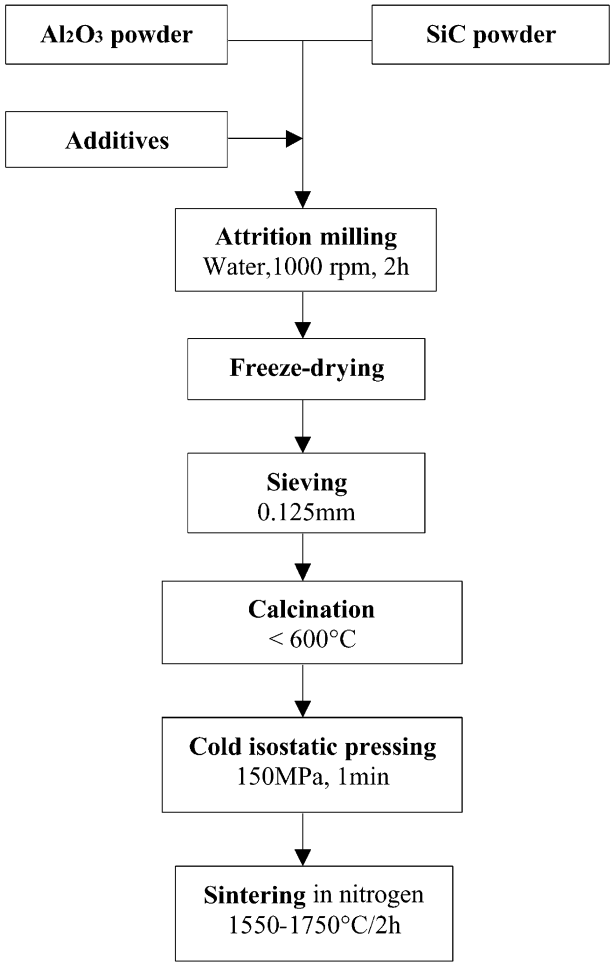

Fig. 1. Process flow chart for the preparation of nanocomposites.

Table 1
Chemical analysis data for UF45 silicon carbide powder (by supplier)

Powder	Chemical analysis (wt.%)				
	Free C	Free Si	Fe	Al	O
UF45	0.58	0.22	0.05	0.03	3.5

technique,[12,24] producing a typical batch of 70 g of nanocomposite. Dried powders were sieved (0.125 mm) and then calcined in air at 600 °C for 4 h in order to remove any contamination introduced during processing and to convert the respective nitrates to oxides. Nanocomposite powders were compacted into cylindrical discs using uniaxial pressing (30 mm diameter die) at 50 MPa pressure, followed by cold isostatic pressing at 150 MPa pressure. The samples were embedded in SiC powder (Grit 400) in a graphite crucible and sintering was carried out in a high temperature graphite element furnace (Thermal Technology Inc., USA), heated to temperatures ranging from 1550 to 1700 °C at 5 °C/min, in a flowing nitrogen atmosphere at 0.1 MPa.

Dilatometric shrinkage experiments were carried out using an attachment to the sintering furnace mentioned above. The attachment consisted of a high temperature, vertical, single push-rod dilatometer having a transducer with 10 mm linear range and a temperature range up to 2000 °C, with control, data acquisition and evaluation via a personal computer. The sample holder system used for these measurements was made of dense graphite. Sample dimensions for the dilatometric study were 8 mm diameter and ~15 mm length and these were uniaxially pressed at 50 MPa pressure and then CIPed at 150 MPa pressure as indicated previously. Nitrogen at 0.1 MPa was used as the atmosphere during the experiment and the heating rate adopted was 10 °C/min.

Densities of the samples were evaluated based on Archimedes' principle. The theoretical density of alumina/5 vol.% silicon carbide was calculated to be 3.94 g cm^{-3} based on the theoretical densities of α-alumina (3.98 g cm^{-3}) and silicon carbide (3.20 g cm^{-3}).

Detailed microstructural examination of the sintered nanocomposites was carried out using Transmission Electron Microscopy (TEM) (JEOL JEM 2010, FASTEM). Specimens for TEM were prepared by first reducing the thickness by surface grinding to ~200 μm. Discs of 3 mm diameter were cut from the ground specimens using a Gatan 601 ultrasonic disc grinder. Discs were mounted on steel stubs and, using a Gatan 623 disc grinder, controlled amounts of material were removed by grinding and polishing. The discs were ground on both sides using progressively finer SiC papers and the surfaces were polished to a 3–6 μm finish using diamond paste which reduced the thickness of the discs to ~80 μm. The polished discs were then dimpled using a Gatan 656 Dimple Grinder and 3–6 μm diamond paste until the centre of the dimple was ~30 μm. Ion beam thinning was carried out on the dimpled discs using a Pfeiffer-Balzers Ion Beam Thinner (IEU100). The incident angle of the ions, initially fixed at 20° was reduced to 15° as thinning progressed. Thinning was stopped when the ions penetrated the material at the centre of the dimple. The thinned, etched samples were carbon coated and examined by TEM.

The average grain sizes of the doped and the undoped nanocomposites were determined from electron micrographs by the linear intercept method.[25] At least 200 grains were counted in each specimen.

Microstructural analysis using a scanning electron microscope (JEOL JSM 840) was carried out on specimens polished down to 1 μm finish and thermally etched at 1400 °C for 1 h. Surface mapping was carried out using a position-tagged spectroscopic (PTS) technique, as an attachment to a high-resolution field emission scanning electron microscope (FESEM, Hitachi, S4300). Specimens were coated with graphite and no thermal etching was carried out on polished samples prior to PTS analysis.

Vickers microhardness measurements (Leco M 400-GI) were carried out on sintered nanocomposites, polished to 1 μm finish. Indentations were made with a load of 10 kg for 30 s. Hardness is calculated from the diagonal length of the impression, using the equation:

$$H_v = 1.8544\frac{P}{\mathrm{d}^2} \quad (1)$$

where, H_v = Vickers hardness, P = applied load (kg) and d = mean of the diagonal length (mm).

Measurements were made immediately after the indentation in order to avoid any difference in crack length due to the environmental variables such as moisture and time. Fracture toughness of the materials was calculated from these measurements. The following equation[26] was used to evaluate the fracture toughness, assuming the crack system to be Palmqvist:

$$K_{ic} = 0.018H^{0.6}E^{0.4}\mathrm{al}^{-0.5} \quad (2)$$

Young's modulus (E) was measured by an ultrasonic technique. Sintered nanocomposites with parallel faces were used. The time taken by a longitudinal wave and a transverse wave (10 MHz ultrasonic pulse) to traverse between the parallel surfaces was measured by an oscilloscope. Young's modulus was calculated based on the following equations:

$$E = \rho\frac{3V_l^2 - 4V_t^2}{\left(\frac{V_l}{V_t}\right)^2 - 1} \quad (3)$$

where, E = Young's modulus (GPa), ρ = density of the sample (g/cm^3), V_l = longtitudinal velocity (m/s), V_t = transverse velocity (m/s).

Erosive wear tests were carried out using a rotary jet slurry wear tester based on a design from the University of Oxford.[23] Samples for erosive wear tests were cut from discs using an Isomet 2000 [Buehler] precision saw. Samples were cut to dimensions of $15\times11.5\times5.4$ mm^3. Samples were first polished with a 40 μm diamond wheel to remove the surface layer. They were then successively polished using 25, 14, 6 and 1 μm diamond slurries. Each specimen is eroded for a total period of 13 h in a slurry consisting of 1.5 kg of SiC (mean particle size ~780 μm) in 8 l of distilled water. A 'fresh' slurry was used for each wear test. All erosive wear tests were performed with an operating speed of 180 rpm, at which the particle impact velocity on the specimen is ~2.4 m/s and the particle flux is $\sim8.6\times10^7$.[23] The weight of each specimen was measured after 1, 4, 7, 10 and 13 h using a high precision balance. Worn surfaces of the nanocomposites were analysed using scanning electron microscopy (Jeol JSM 840).

3. Results and discussion

3.1. Densification behaviour

Dilatometry is ideally suited to study shrinkage during firing. Fig. 2 shows the dilatometric curves of shrinkage rate v. temperature for the doped Al_2O_3–5 vol.% SiC nanocomposites (1Mg–NC, 1Y–NC and 1Ce–NC) in comparison with that of the undoped nanocomposite (NC).

Sintering starts at about 1150 °C for all the nanocomposites and continues at similar rates to 1250 °C with a slightly lower rate for 1Ce–NC. Above 1250 °C, the sintering rate for NC increases more slowly than for the doped nanocomposites. The sintering rates for 1Mg–NC and 1Y–NC are higher in the range 1250 to 1350 °C and, above 1350 °C, 1Y–NC has the highest shrinkage rate up to 1450 °C after which it decreases. Above this temperature range, the densification rate of 1Mg–NC decreases and is lower than that of NC. The highest shrinkage rates for 1Mg–NC occur at ~1300 and 1500 °C and for 1Y–NC at 1450 °C whereas for 1Ce–NC and NC, these occur at 1450 and 1600 °C.

From the chemical analysis data (Table 1), it is known that each powder particle of the nanophase SiC has silica present on its surface. In the case of NC, this reacts with alumina above ~1600 °C to form a liquid phase at the grain boundaries. In the case of the doped nanocomposites, the extra oxide dopant will lower the liquidus temperature to 1355 °C in the case of MgO–Al_2O_3–SiO_2,[27] and a similar liquidus temperature for the alumina–yttria–silica system.[28] The decrease in densification for MgO at ~1400 °C could be accounted for by the formation of spinel ($MgAl_2O_4$), which retards the alumina grain boundary movement by pinning.

In order to study the effect of MgO, Y_2O_3 and CeO_2 on the densification of NC at particular temperatures, a sintering study was carried out between 1550 and 1700 °C for 2 h. From Fig. 3, it can be seen that, in order to achieve densities of >98.5%, a temperature of 1700 °C is required for the undoped nanocomposite. The addition of MgO or CeO_2 allows this level of densification to be achieved at ~1650 °C. At 1550 °C, 1Y–NC yielded ~99% theoretical density compared to 92% density for the undoped nanocomposite, NC. Above 1600 °C, the density of 1Y–NC showed a slight decrease.

The use of dopants allows pressureless sintering of the nanocomposites to be carried out at much lower temperatures and this affects the microstructure, particularly grain size.

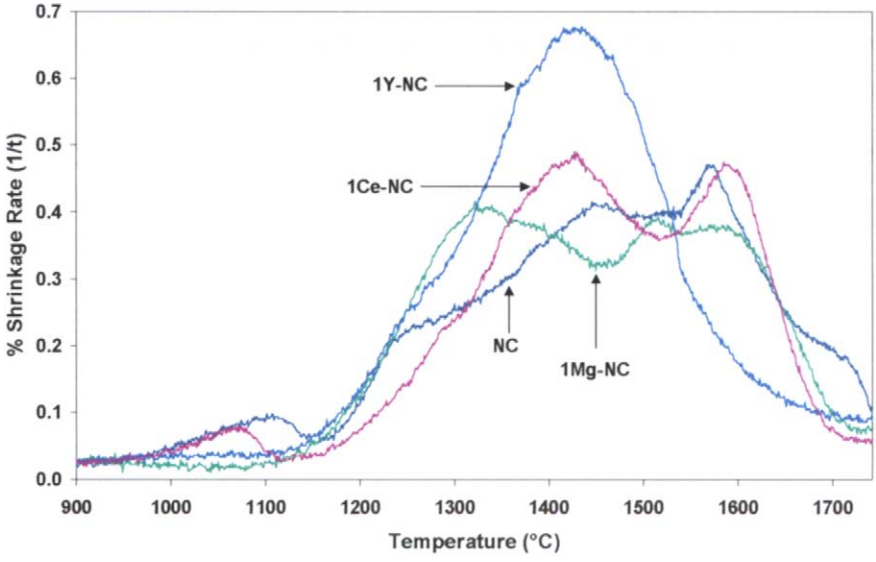

Fig. 2. Dilatometric shrinkage rate vs. temperature curves for NC, 1Mg–NC, 1Y–NC and 1Ce–NC.

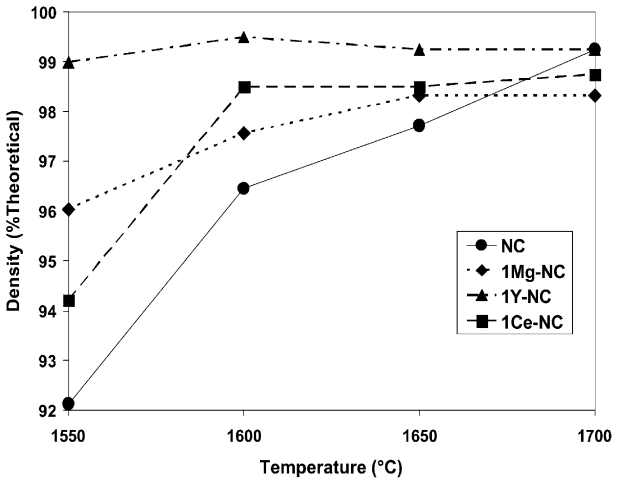

Fig. 3. Densification behaviour of undoped nanocomposite (NC) in comparison with 1Mg–NC, 1Y–NC and 1Ce–NC doped nanocomposites.

3.2. Microstructural analysis

In order to ascertain the microstructural characteristics which lead to differences in mechanical properties, NC, 1Y–NC and 1Ce–NC nanocomposites were further analysed by transmission electron microscopy. Fig. 4 shows a bright field image and a diffuse dark field image of the undoped nanocomposite sintered at 1700 °C which reveal the presence of an amorphous phase and a SiC particle, marked at U with high aspect ratio. Neighbouring intergranular SiC particles can be seen at E and F, and an intragranular SiC agglomerate at G. Large intergranular amorphous 'pools' are observed at V and W. These amorphous phases are the result of liquid phase formation at high temperatures from the reaction of impurities and silica with alumina.

Fig. 5 is a through focal series of bright field images of the 1Y–NC sintered at 1700 °C that demonstrate the way in which the grain boundary in alumina is associated with an amorphous phase. Note for example, the 'dark–light–dark' contrast in the area marked at V (where the amorphous phase has a thickness of some 1.5 nm), which is indicative of the fact that the boundary is of lower scattering potential than the crystalline alumina grains lying to its immediate sides. The critical point, however, is the way in which the boundary exhibits such a strong absorption contrast in the close to focus image, which indicates that the boundary is enriched with a relatively high atomic number species, that is, yttrium. No yttrium containing particles, such as YAG, were seen in the area analysed. The 1Y–NC nanocomposite densified to near-full density at less than 1600 °C and the enhancement in densification can be attributed to the presence of liquid phase at the sintering temperature, formed by lower temperature reactions of alumina and yttria with the surface silica from the SiC powder. However, the grain size is much higher

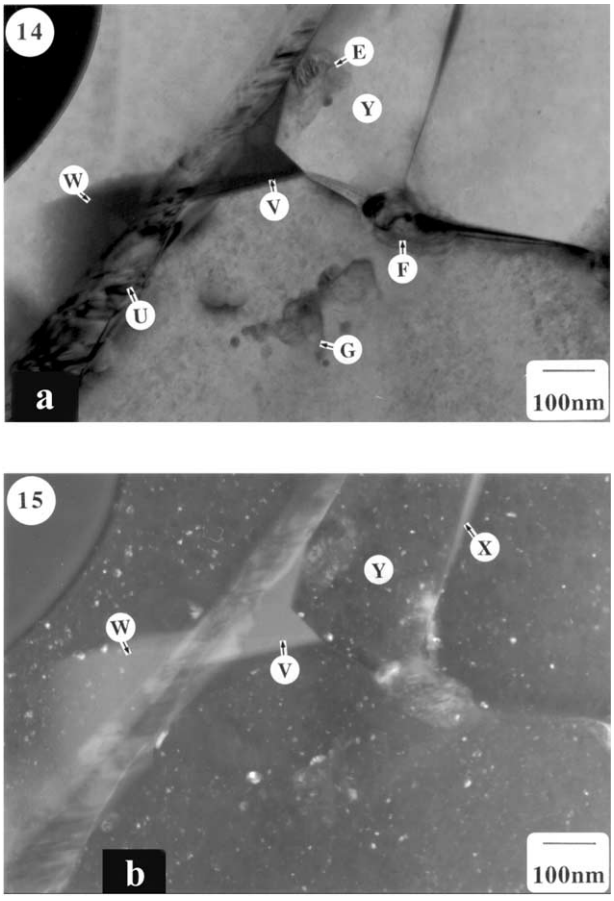

Fig. 4. (a) Bright field image of NC showing SiC at intergranular positions (E and F), intragranular position (G), SiC with high aspect ratio (U) and amorphous 'pools' (V and W) and (b) diffuse dark field image showing amorphous 'pools' at V and W.

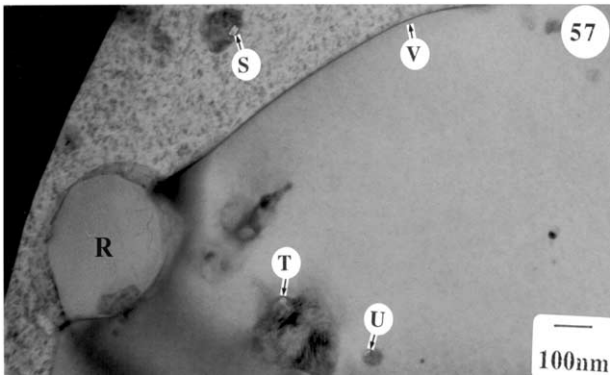

Fig. 5. Bright field TEM image of 1Y–NC, showing the grain boundaries of alumina associated with amorphous layer at V (S, T and U are the pores in SiC).

than for NC or the other doped nanocomposites. PTS mapping of 1Y–NC, sintered at 1600 °C and polished to 1 μm is shown in Fig. 6. SiC particles are reasonably well distributed in the alumina matrix including within the alumina grains. However, Y_2O_3 is distributed mainly along the grain boundaries. This distribution can be seen more clearly in the enlarged FESEM image

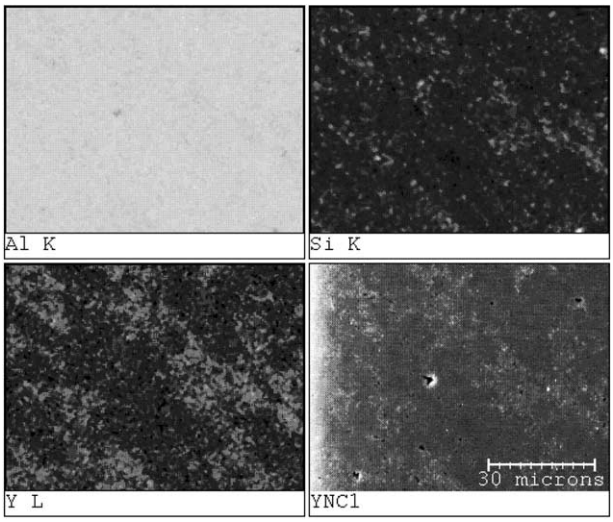

Fig. 6. PTS mapping of 1Y–NC showing Si and Y distributions.

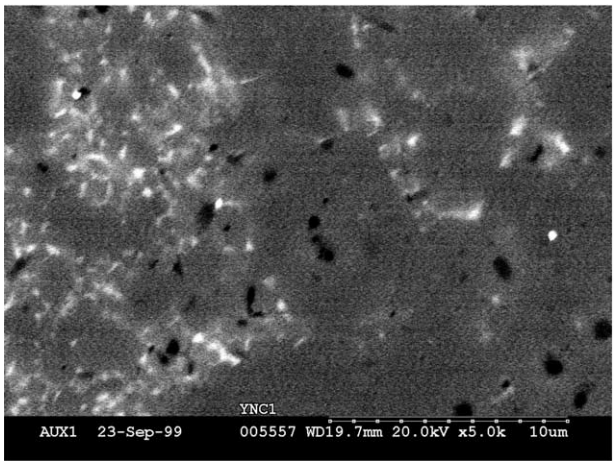

Fig. 7. Enlarged FESEM image showing the grain boundary precipitation in 1Y–NC sintered at 1600 °C for 2 h.

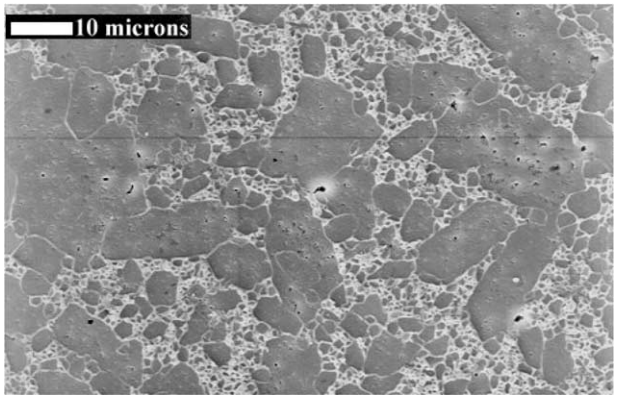

Fig. 8. SEM image of 1Y–NC sintered at 1600 °C for 2 h showing abnormal grain growth of matrix alumina.

of the scanned area shown in Fig. 7 which also shows grain boundary precipitation.

The main factors which control the solubility of solute in a solvent include: (1) the elastic strain due to the difference in atomic sizes (ionic radius of Al^{3+} is 0.5 Å and that of Y^{3+} is 0.93 Å), and (2) the mismatch between crystallographic structures of the two equilibrium phases (the electronic charge associated with each species is the same in this case).[15] In the yttria- alumina system, yttria has been reported at the grain boundaries[29,30] and at the free surfaces.[31] Cawley and Halloran[32] evaluated the solubility limit of yttria in alumina to be 10 ppm by mass at 1600 °C. Hence, the remaining yttria migrates to the grain boundaries. During sintering, the grain boundary solute content increases due to the diminution of the area of grain boundary per unit volume. When the solubility limit at the grain boundaries (which is higher than the bulk) is reached, the boundaries become oversaturated and, if grain growth continues, yttria can not be accommodated in solid solution at the grain boundaries and therefore forms another phase instead. X-ray diffraction analysis was carried out on the 1Y–NC sample to check for the formation of any new phases. However, no other phase could be detected and, at the level of formation expected, the quantity of any other phase formed is below the detectable range of the XRD instrument.

The grain boundaries in 1Y–NC sintered at 1600 °C can be seen more clearly in Fig. 8 which shows a bimodal grain size distribution with very large grains surrounded by smaller grains. The elongated, lath-like grains with flat crystallographic faces and non-equilibrium dihedral angles clearly indicate the effect of liquid phase sintering. In the presence of glass forming impurities (here, silica), the concentration of Y per unit area of grain boundary continued to increase in the final stage of densification as grains grew. When the impurity content at the grain boundary attained a critical level, liquid phases of thermodynamically stable thickness could form and induce a sudden increase in the mobility of grain boundaries that were wetted by the liquid film at higher temperature thus resulting in the observed abnormal grain growth.

A typical microstructure of the 1Ce–NC nanocomposite sintered at 1650 °C is shown in the TEM image of Fig. 9. It can be seen that the grain size of the matrix alumina is much lower than that of the undoped nanocomposite and, particularly, the 1Y–NC nanocomposite. The dislocation density is also higher than in the NC and 1Y–NC nanocomposites. The intergranular regions between alumina grains in the 1Ce–NC nanocomposite were examined in detail and were found to be quite different to those described for NC and 1Y–NC. One such area is shown in the pair of bright and dark field images in Fig. 10(a) and (b) and it is immediately apparent that a large pool of amorphous material has been formed at the intersection of the different alumina grains (as at S). The diffuse dark field image shown in Fig. 10(b) confirms the amorphous nature of the pool

and also demonstrates the way in which it extends out to the region marked at T. The grain boundaries marked at U, V and W were similarly found to be associated with amorphous films extended from their region at S and, in this respect, 1Ce–NC is rather different to that described for NC.

The PTS analysis of 1Ce–NC sintered at 1650 °C, presented in Fig. 11 shows both SiC and CeO_2 distributed mainly around the grain boundaries. The SiC particles are coarser in size. A probable role of grain boundary CeO_2 in such a coarsening of SiC cannot be ruled out. CeO_2 distribution around the matrix alumina grain boundary can be seen more clearly on an enlarged FESEM image shown in Fig. 12. Such a large amount of dopant at the alumina matrix grain boundary can have a major significance in refining the grain size of alumina. The etched surface of 1Ce–NC sintered at 1650 °C shown in the scanning electron micrograph of Fig. 13 exhibits a reasonably refined microstructure with an average grain size of ~2.3 μm.

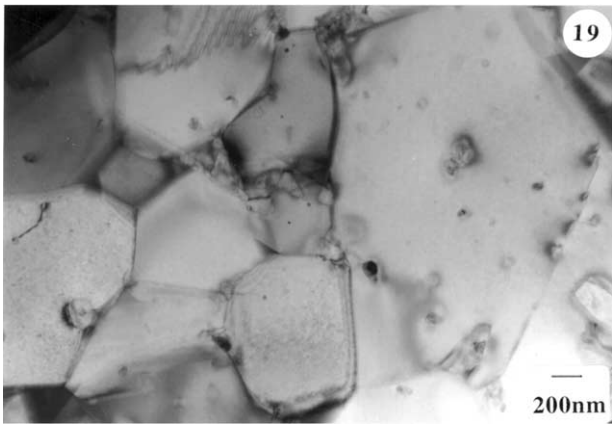

Fig. 9. Bright field TEM image of 1Ce–NC showing finer grain size compared to NC and 1Y–NC.

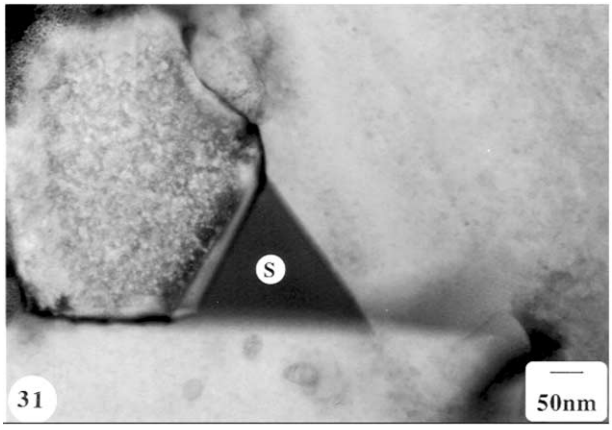

(a)

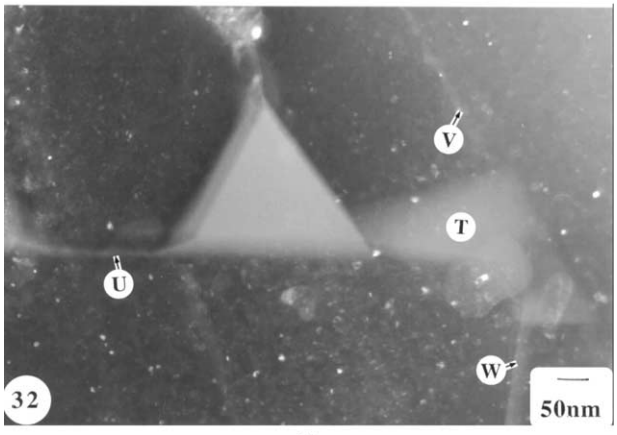

(b)

Fig. 10. (a) Bright field and (b) diffuse dark field TEM images of 1Ce–NC showing intergranular pool of amorphous material at S and its extension at T. U, V and W are grain boundaries associated with amorphous layers.

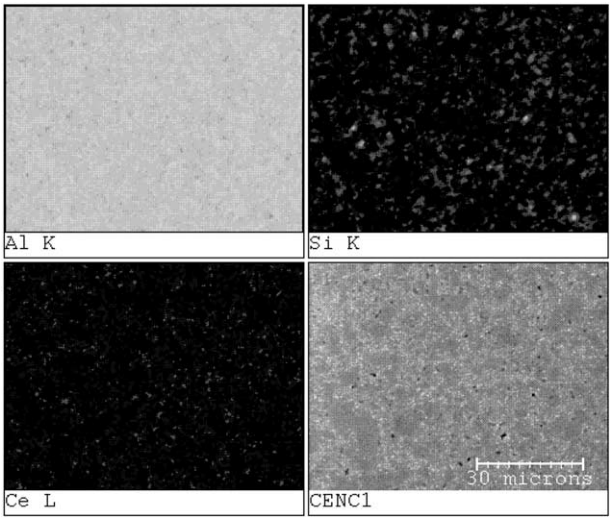

Fig. 11. PTS mapping of 1Ce–NC showing Si and Ce distributions.

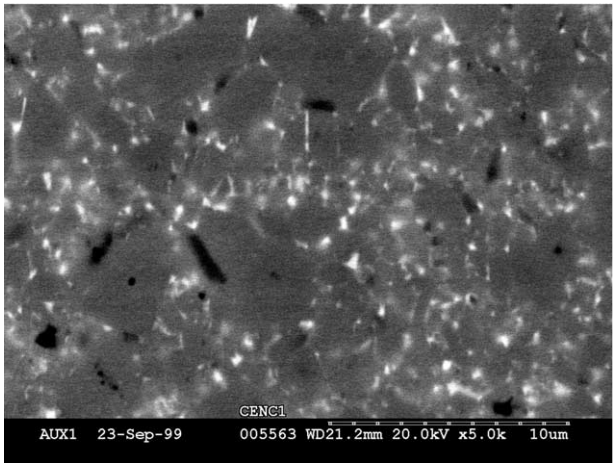

Fig. 12. Enlarged FESEM image of 1Ce–NC showing ceria distribution at the grain boundaries.

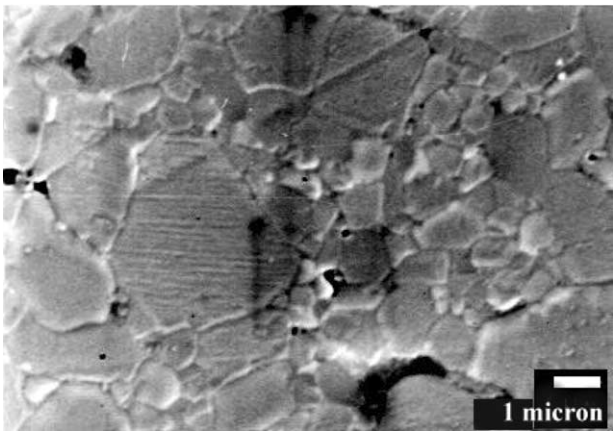

Fig. 13. SEM image of etched surface of 1Ce–NC showing smaller grain size distribution.

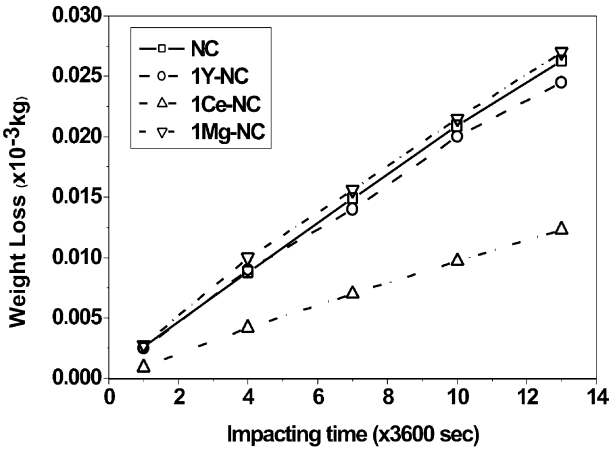

Fig. 14. Erosive wear behaviour of undoped and doped nanocomposites.

3.3. Mechanical properties

Table 2 shows the Young's modulus, hardness and fracture toughness values of the undoped and doped nanocomposites fabricated at various sintering temperatures to achieve densities of >98.5% theoretical. The Young's modulus for the undoped nanocomposite (NC) was 400 GPa and values for the doped nanocomposites were lower, in the range 385–392 GPa. The fracture toughness of the undoped nanocomposite was 4.63 MPa.m$^{0.5}$ with 1Mg–NC and 1Y–NC having slightly lower values and 1Ce–NC a slightly higher value. Hardness of the undoped nanocomposite was 16.44 GPa and among the doped nanocomposites, 1Ce–NC yielded the highest hardness value at 17.21 GPa.

Erosive wear results for the doped nanocomposites are compared with the undoped nanocomposite in Fig. 14. 1Y–NC and 1Mg–NC showed similar wear behaviour to the undoped nanocomposite whereas, after 13 h test, the 1Ce–NC yielded almost 2.5 times higher erosive wear resistance than the other nanocomposites. Fig. 15 shows scanning electron micrographs of worn surfaces of doped and undoped nanocomposites after 13 h of testing. Pitting is observed in the NC which could have been caused by tensile stresses in the matrix close to SiC particles which are particularly significant when SiC particles are clustered due to agglomeration during processing. Similar observations have also been reported by Chen et al.[33] When compared with the undoped nanocomposite, the 1Ce–NC material has a smoother surface, suggesting the operation of a non-selective, uniform material removal mechanism that has been attributed previously to the tribochemical solution of alumina into the aqueous phase accelerated by the transfer of energy from impacting SiC grit particles. A contribution from local plastic deformation is also

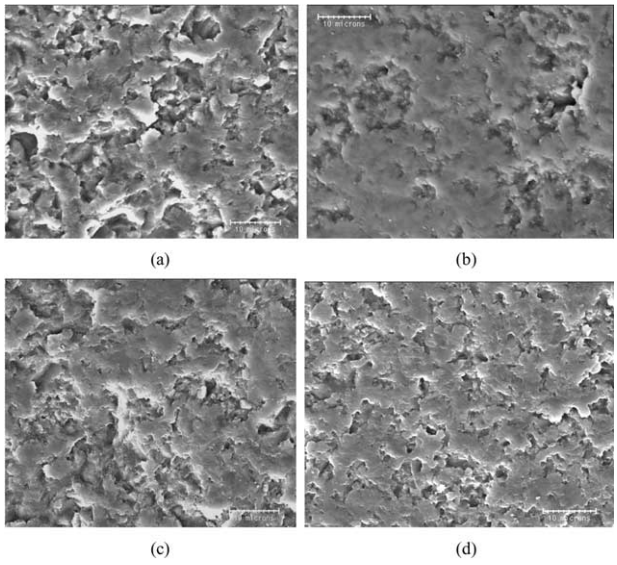

Fig. 15. Scanning electron micrographs of worn surfaces of (a) NC, (b) 1Mg–NC, (c) 1Y–NC and (d) 1Ce–NC, after 13 h erosive wear test.

Table 2
Density (ρ), hardness (H), Young's modulus (E) and fracture toughness (K_{1c}) values of undoped nanocomposite and doped nanocomposites

Sample	ρ (% theoretical)	H (GPa)	E (GPa)	K_{1C} palmqvist (MPa m$^{0.5}$)
NC–1700/2 h	99.2	16.44±0.21	400	4.63±0.22
1MgO–NC–1650/2 h	98.9	16.76±0.22	385	4.43±0.08
1Y_2O_3–NC–1600/2 h	99.5	16.52±0.32	396	4.59±0.12
1CeO_2–NC–1650/2 h	98.5	17.21±0.29	392	4.71±0.12

possible.[34] The major fracture mode is transgranular and intergranular fracture was not observed in any of the samples.

In general, it can be concluded that the improvement in wear resistance of the 1Ce–NC nanocomposite over undoped nanocomposite is due to the following reasons:

1. Increased amounts of compressive residual stresses, as evidenced by the presence of more dislocations and extensive subgrain formation.
2. Amorphous phases at triple points and along grain boundaries.
3. Grain boundary strengthening by the presence of amorphous phases.
4. Refinement in grain size caused by the ceria addition.
5. The presence of fine pores which can absorb the energy of impacting particles.

4. Conclusions

Alumina–5 vol.% silicon carbide nanocomposites can be prepared by an aqueous processing route consisting of attrition milling and freeze-drying followed by pressureless sintering to near-theoretical density at 1700 °C for 2 h. By using oxide dopants, MgO, Y_2O_3 and CeO_2, the sintering temperature of the nanocomposite can be significantly reduced from 1700 to 1550 °C in the case of Y_2O_3 addition (1 wt.%), but exaggerated grain growth of the alumina occurs. MgO and CeO_2 additions also reduce the effective sintering temperature to ~1600 °C and restrict the grain growth of the matrix alumina. In the MgO doped nanocomposite, spinel was formed at three grain junctions whereas, in both Y_2O_3 and CeO_2 doped nanocomposites, the dopants were segregated mostly at the grain boundaries. Early densification in the case of all these doped nanocomposites is attributed to the formation of liquid phases due to the dopant reaction with the matrix alumina and the excess silica present on the SiC powder surface.

Mechanical properties (Young's modulus, hardness, fracture toughness and erosive wear resistance) have been evaluated and compared with the undoped nanocomposites. The erosive wear resistance of Ce-doped nanocomposites is some 2.5 times higher than for the undoped and Mg- or Y-doped nanocomposites. Improvement in wear resistance of the 1Ce–NC nanocomposite over the other nanocomposites is due to increased amounts of compressive residual stresses, as evidenced by the presence of more dislocations and extensive subgrain formation, amorphous phases at triple points and along grain boundaries causing grain boundary strengthening and refinement in grain size.

Acknowledgements

The authors would like to acknowledge financial support from the European Commission under BRITE EURAM Contract no: BRPR CT96 0212 NACATA and to thank Dr. David O'Sullivan for acting as coordinating secretary for the project. Dr. Steve Roberts, Department of Materials, University of Oxford, is thanked for advice, useful discussions and use of erosive wear tester. We are grateful to Dr. Simon Newcomb for providing Transmission Electron Micrographs of the samples.

References

1. Niihara, K. and Nakahira, A., Particulate strengthened oxide ceramics- Nanocomposites. In *Advanced Structural Inorganic Composites*, ed. P. Vincenzini. Elsevier Science, 1991, pp. 637–644.
2. Niihara, K., New design concept of structural ceramics–Ceramic nanocomposites. *J. Ceram. Soc, Jpn.*, 1991, **99**, 974–982.
3. Zhao, J., Stearns, L. C., Harmer, M. P., Chan, H. M., Miller, G. A. and Cook, R. F., Mechanical behaviour of alumina–silicon carbide "nanocomposites". *J. Am. Ceram. Soc.*, 1993, **76**, 503–510.
4. Borsa, C. E., Jiao, S., Todd, R. I. and Brook, R. J., Processing and properties of Al_2O_3/SiC nanocomposites. *J. Microscopy*, 1995, **177**, 305–312.
5. Davidge, R. W., Brook, R. J., Cambier, F., Poorteman, M., Leriche, A., O'Sullivan, D., Hampshire, S. and Kennedy, T., Fabrication, properties and modelling of engineering ceramics reinforced with nanoparticles of silicon carbide. *J. Eur. Ceram. Soc.*, 1996, **16**, 799–802.
6. Anya, C. C. and Roberts, S. G., Indentation fracture toughness and surface flaw analysis of sintered alumina/SiC nanocomposites. *J. Eur. Ceram. Soc.*, 1996, **16**, 1107–1114.
7. Sternitzke, M., Derby, B. and Brook, R. J., Alumina/silicon carbide nanocomposites by hybrid polymer/powder processing: microstructures and mechanical properties. *J. Am. Ceram. Soc.*, 1998, **81**, 41–48.
8. Schmid, H. K., Aslan, M., Assmann, S., Naβ, R. and Schmidt, H., Microstructural characterisation of Al_2O_3–SiC nanocomposites. *J. Eur. Ceram. Soc.*, 1998, **18**, 39–49.
9. Levin, I., Kaplan, W. D., Brandon, D. G. and Layyous, A. A., Effect of SiC submicrometer particle size and content on fracture toughness of alumina–SiC nanocomposites. *J. Am. Ceram. Soc.*, 1995, **78**, 254–256.
10. Assmann, S., Eisele, U. and Boder, H., Processing of Al_2O_3/SiC composites in aqueous media. *J. Eur. Ceram. Soc.*, 1997, **17**, 309–317.
11. Piciacchio, A., Lee, S.-H. and Messing, G. L., Processing and microstructure development in alumina–silicon carbide intragranular particulate composites. *J. Am. Ceram. Soc.*, 1994, **77**, 2157–2164.
12. Baron, B., Kumar, C. S., Le Gonidec, G. and Hampshire, S., Comparison of different alumina powders for the aqueous processing and pressureless sintering of Al2O3–SiC nanocomposites. *J. Eur. Ceram. Soc.*, 2002, **22**(9–10), 1543–1552.
13. Powers, J. D. and Glaeser, A. M., Grain boundary migration in ceramics. *Interface Science*, 1998, **6**, 23–39.
14. Coble, R. L., Sintering crystalline solids: I. Intermediate and final stage diffusion models. *J. Appl. Phys.*, 1961, **32**, 787–792.
15. Gruffel, P. and Carry, C., Effect of grain size on yttrium grain boundary segregation in fine-grained alumina. *J. Eur. Ceram. Soc.*, 1993, **11**, 189–199.
16. Bae, I-J. and Baik, S., Densification of critical concentration of

silica and/or calcia for abnormal grain growth in alumina. *J. Am. Ceram. Soc.*, 1993, **76**, 1065–1067.
17. Wang, J., Lim, S. Y., Ng, S. C., Gan, L. M. and Chew, C. H., Dramatic effect of a small amount of MgO addition on the sintering of Al_2O_3–5 vol.% SiC nanocomposite. *Mater. Lett.*, 1998, **33**, 273–277.
18. Jeong, Y. K., Nakahira, A. and Niihara, K., Effects of additives on microstructure and properties of alumina–silicon carbide nanocomposites. *J. Am. Ceram. Soc.*, 1999, **82**, 3609–3612.
19. Pillai, S. K. C. and Hampshire, S., Controlling the grain growth in yttria-doped Al2O3–5 vol.% SiC nanocomposites prepared by pressureless sintering. (Submitted to *J. Am. Ceram. Soc.*).
20. Borsa, C. E., Ferreira, H. S. and Kiminami, R. H. G. A., Liquid phase sintering of Al_2O_3/SiC. *J. Eur. Ceram. Soc.*, 1999, **19**, 615–621.
21. Davidge, R. W., Twigg, P. C. and Riley, F. L., Effects of silicon carbide nano-phase on the wet erosive wear of polycrystalline alumina. *J. Eur. Ceram. Soc.*, 1996, **16**, 799–802.
22. Twigg, P. C., Davidge, R. W., Roberts, S. G. and Riley, F. L., Factors affecting the wet erosive wear of liquid sintered aluminas. In *Key Engineering Materials*, Vols. 132–136, Trans Tech Publications, Switzerland, 1997, pp. 1524-1527.
23. Franco, A. and Roberts, S. G., Controlled wet erosive wear of polycrystalline alumina. *J. Eur. Ceram. Soc.*, 1996, **16**, 1365–1375.
24. Kennedy, T., Poorteman, M., Cambier, F. and Hampshire, S., Silicon nitride–silicon carbide nanocomposites prepared by water processing of commercially available powder. *J. Eur. Ceram. Soc.*, 1997, **17**, 1917–1923.
25. Mendelson, M. I., Average grain size in polycrystalline ceramics. *J. Am. Ceram. Soc.*, 1969, **52**, 443–446.
26. Niihara, K., Morena, R. and Hasselman, D. P. H., Evaluation of K_{ic} of brittle solids by the indentation method with low crack-to-indent ratios. *J. Mater. Sci. Lett.*, 1982, 13–16.
27. E. M. Levin, C. R. Robbins and H. K. McMurdie (eds), *Phase Diagrams for Ceramists*, American Ceramic Society, Inc., 1964.
28. Levin E. M., Robbins C. R. and McMurdie H. K (eds). *Phase Diagrams for Ceramists*, American Ceramic Society, Inc., 1969.
29. Li, C. W. and Kingery, W. D., Solute segregation at grain boundaries in polycrystalline Al_2O_3. In *Advances in Ceramics*, ed. W. D. Kingery. American Ceramic Society, Columbus OH, 1985.
30. Bender, B., Williams, D. B. and Notis, M. R., Investigation of grain–boundary segregation in ceramic oxides by analytical scanning transmission microscopy. *J. Am. Ceram. Soc.*, 1980, **63**, 542–546.
31. Lagrange, M. H., Huntz, A. M. and Laval, J. Y., Effect of yttrium on the microstructure and diffusion properties of α-alumina. *Ann. Chim. Fr.*, 1987, **12**, 9–21.
32. Cawley, J. D. and Halloran, J. W., Dopant distribution in nominally yttrium-doped sapphire. *J. Am. Ceram. Soc.*, 1986, **69**, C195–C196.
33. Chen, H. J., Rainforth, W. M. and Lee, W. E., The wear behaviour of Al_2O_3–SiC ceramic nanocomposites. *Scripta Materialia*, 2000, **42**, 555–560.
34. Martinez, M-.M., Davidge, R. W. and Riley, F. L., Grain size effects on the wet erosive wear of high-purity crystalline alumina. *Wear*, 1994, **172**, 41–48.